

A Highly Reversible Aqueous Ammonium-Ion Battery based on α -MoO₃/Ti₃C₂T_z Anodes and (NH₄)_xMnO₂/CNTs Cathodes

Li Yang,^[a, b] Wei Zheng,^[c] Joseph Halim,^[b] Johanna Rosen,^{*[b]} ZhengMing Sun,^{*[a]} and Michel W. Barsoum^{*[b, d]}

Aqueous ammonium-ion batteries (AAIBs) are appealing due to their relatively low cost and good rate performance. In general, AAIBs are environmentally friendlier than their non-aqueous counterparts. However, it is still a challenge to achieve highly reversible AAIBs with decent voltages and energy/power densities. Herein, we report on a full-cell configuration using α -MoO₃/Ti₃C₂T_z films as anodes, and (NH₄)_xMnO₂/CNTs films as cathodes in a 1 M ammonium acetate (NH₄Ac) electrolyte. At 2 V, the operating cell voltage, OCV, is one of the highest reported for AAIBs. A maximum energy density of \sim 32 Wh kg⁻¹

(\sim 54 Wh L⁻¹) at 0.2 Ag⁻¹ and a maximum power density of \sim 10 kW kg⁻¹ (\sim 17 kW L⁻¹) at 10 Ag⁻¹ are attained. When the full cells are cycled 2,000 times at 1 Ag⁻¹ they retain \sim 73 % of their initial capacity. When cycling at 10 Ag⁻¹, \sim 96 % of capacity is retained after 43,500 cycles. After 10 h, self-discharge reduces the OCV to \sim 72 % of its original value. This work provides a roadmap for developing high performance AAIBs with high voltages and high energy/power densities. Before this is possible it is imperative that the self-discharge rate be substantially reduced.

Introduction

Aqueous ammonium-ion batteries (AAIBs) are attractive because of the small hydrated ionic size (3.31 Å) of NH₄⁺ that facilitates fast ion diffusion and reduced corrosiveness compared with acidic/alkaline electrolytes.^[1] Pioneering work on AAIBs was first reported by the Cui group.^[1a] Since then, promising results have been achieved towards developing new anodes and cathodes for AAIBs.^[1b, 2] However, reports on full cells are still few and far between, and the operating cell voltages (OCVs), energy densities and cyclic stabilities could be improved upon.

Metal-based compounds and organic materials have been used as anode materials for AAIBs.^[2, 3] For example, hexagonal molybdenum trioxide (*h*-MoO₃) nanobelts with a tunnel structure, provide faster diffusion pathways and ultra-fast kinetics for hosting NH₄⁺ ions than α -MoO₃.^[2a] As a result, a reversible capacity of 32 mAh g⁻¹ at 15 Ag⁻¹ with 94 % capacity retention over 100,000 cycles was achieved. However, *h*-MoO₃ is metastable, and its synthesis is more complex than other MoO₃ polymorphs.^[2b] Herein, we are more interested in the layered, thermodynamically stable orthorhombic MoO₃, *viz.* α -MoO₃, with space group Pcmn and lattice parameters *a* = 3.963 Å, *b* = 3.696 Å, *c* = 13.855 Å. This oxide is comprised of two layers of [MoO₆] octahedra that share corners along the *b* axis and share edges along the *c* axis.^[4] However, the low capacities and low electronic conductivities of the electrodes made with this oxide represent serious obstacles.^[2a]

MXenes, a relatively new group of 2D transition metal carbides/nitrides, with large interlayer spacings, have proven to be excellent hosts for various cations due to their high electronic conductivities and hydrophilicity.^[5] We have previously shown that introducing Ti₃C₂T_z MXene into α -MoO₃ anodes greatly enhances the electronic conductivity of the electrodes.^[6] Building on that work, herein we fabricated α -MoO₃/Ti₃C₂T_z free-standing films and tested them as anodes for AAIBs.

Cathode materials also play a crucial role in determining the capacity and cycling stability of full AAIBs. Prussian blue analogues (PBAs) are some of the most common cathodes in AAIBs. However, this cathode results in low specific capacities and/or rapid fading in capacity upon cycling.^[7] It follows that alternative cathode materials with better electrochemical performances need to be developed. Mn-based compounds have shown good potential for hosting NH₄⁺ cations.^[8] Particularly, it has been shown that birnessite, or layered δ -

[a] L. Yang, Z. Sun
School of Materials Science and Engineering
Southeast University
Nanjing 211189 (P.R. China)

E-mail: zmsun@seu.edu.cn

[b] L. Yang, J. Halim, J. Rosen, Prof. M. W. Barsoum
Department of Physics, Chemistry and Biology (IFM)
Linköping University
Linköping 581 83 (Sweden)

E-mail: johanna.rosen@liu.se

[c] W. Zheng
School of Chemistry and Chemical Engineering
Southeast University
Nanjing 211189 (P.R. China)

[d] Prof. M. W. Barsoum
Department of Materials Science and Engineering
Drexel University
Philadelphia 19104, Pennsylvania (USA)

E-mail: barsoumw@drexel.edu

 Supporting information for this article is available on the WWW under
<https://doi.org/10.1002/batt.202200432>

 © 2022 The Authors. *Batteries & Supercaps* published by Wiley-VCH GmbH.
This is an open access article under the terms of the Creative Commons Attribution License, which permits use, distribution and reproduction in any medium, provided the original work is properly cited.

MnO_2 , can be directly intercalated with cations without severe structural conversion due to the existence of interlayer water and cations between layers.^[9] Several reports have explored the storage capacity of NH_4^+ in MnO_x . Lu et al. reported MnO_x with a layered structure delivered a high specific capacity of 176 mAh g^{-1} at the current density of 0.5 A g^{-1} .^[8a] Chen et al. demonstrated that $\delta\text{-MnO}_2$ had an ultra-high areal capacity of 2.64 mAh cm^{-2} at 2 mA cm^{-2} in $(\text{NH}_4)_2\text{SO}_4$.^[8b] Another issue with current cathodes is that most of them lack NH_4^+ cations in their native structure, leading to the consumption of NH_4^+ during the first few cycles as these cations intercalate between the layers.^[10]

Very recently, we reported on a bottom-up approach to convert 5 different Mn-bearing precursors, viz. Mn_3O_4 , Mn_2O_3 , MnB , Mn_2AlB_2 and Mn_5SiB_2 to MnO_2 birnessite, by placing them in tetramethylammonium hydroxide (TMAH) aqueous solutions at 50 °C to 80 °C for 4–2 days, respectively. Once the reaction products were washed and filtered, they yielded flexible films comprised of 2D birnessite flakes.^[11] This technique is inexpensive and eminently scalable, with high yields. This 2D birnessite may provide an opportunity to host NH_4^+ owing to the large interlayer spacing and energetically favorable NH_4^+ storage based on a previous report.^[8a]

The purpose of this work is to report on the electrochemical performances of half and full AAIB cells. The cathode is comprised of NH_4^+ -containing birnessite flakes, with 20 wt.% CNTs additives. The anode, on the other hand, is an $\alpha\text{-MoO}_3/\text{MXene}$ composite fabricated in a similar way as in our previous work.^[6] The electrolyte is one molar ammonium acetate, 1 M NH_4Ac and the OCV is 2 V. This value is the highest voltage reported among AAIBs to date. As shown below these cells exhibit good rate performance and excellent cycling stability. The power and energy densities are also respectable.

Experimental Section

Material preparation

Preparation $\alpha\text{-MoO}_3/\text{Ti}_3\text{C}_2\text{T}_z$ films: As noted above, the procedure for making these films can be found in our previous work^[6] and in Supporting Information. In brief, to fabricate composite films, 2 mL of a $\text{Ti}_3\text{C}_2\text{T}_z$ suspension (2 mg mL^{-1}) was slowly added into 8 mL of $\alpha\text{-MoO}_3$ suspension (2 mg mL^{-1}) for a final mass ratio of 2:8. We have previously shown that this ratio was optimum.^[6] After 1 h of vigorous vortex shaking (Sigma-Aldrich, CLS6776, Corning® LSE™), the homogeneous suspension was vacuum filtered through a membrane (Celgard 3501, 0.064 μm pore size, Celgard LLC) to produce $\alpha\text{-MoO}_3/\text{Ti}_3\text{C}_2\text{T}_z$ films. The films obtained were stored in a glove box (Jacomet GP Campus T2, 99.999% purity argon, Ar, atmosphere, $\text{H}_2\text{O} < 1 \text{ ppm}$, $\text{O}_2 < 1 \text{ ppm}$) to prevent possible oxidation.

Preparation of $(\text{NH}_4)_x\text{MnO}_2/\text{CNTs}$ films: The details for preparing 2D birnessite flakes can be found in reference.^[11] In short, 1 g of Mn_3O_4 powder (Sigma-Aldrich, 97%, Sweden) was first added to 20 mL of TMAH solution (25 wt.% in H_2O , Sigma-Aldrich, Sweden) in a 50 mL polyethylene bottle. The resulting brown mixture was magnetically stirred at 500 rpm for 48 h at 80 °C. After the reaction, a dark brown sediment was obtained after carefully rinsing with ethanol for 3 cycles. After the ethanol wash, 40 mL of deionized, DI, water was

added to the sediment and the mixture was sonicated at 100 W (USC 500 T, VWR part of Avantor, Sweden) for 1 hour. Two centrifugation steps – one at 3500 rpm for 20 min followed by another at 6000 rpm for an additional 10 min – were used to collect high-purity TMA^+ intercalated MnO_2 , henceforth labeled T-MnO_2 .

The T-MnO_2 suspension was mixed with a CNTs suspension (single-wall CNTs in water, 0.1 wt.%, Suzhou Tanfeng Tech Co., Ltd, P. R. China) with a mass ratio of 8:2, respectively. The resulting mixture was filtered using Celgard filters to obtain $\text{T-MnO}_2/\text{CNTs}$ free-standing films, that were air dried.

To prepare $(\text{NH}_4)_x\text{MnO}_2/\text{CNTs}$ free-standing films, 6 mm in diameter $\text{T-MnO}_2/\text{CNTs}$ discs were immersed in 10 mL of 1 M NH_4Ac solution for 10 min. The discs were washed with DI water and dried in a fume hood for 2 h. As discussed below, this procedure rapidly replaces the TMA^+ with NH_4^+ cations. We measured the mass of MnO_2/CNTs discs before and after soaking in 1 M NH_4Ac and found no noticeable change. The $(\text{NH}_4)_x\text{MnO}_2/\text{CNTs}$ samples will henceforth be referred to as $\text{N-MnO}_2/\text{CNTs}$.

Materials characterization

X-ray diffraction, XRD, (PANalytical X'Pert diffractometer, Netherlands) was used to characterize samples' phases using Cu K_α (45 kV, 40 mA) in the 3°–70° 2θ ranging with a step size was 0.02° and a scan rate of 0.5 s/step. *Ex-situ* XRD of the full cells' electrodes was measured at different voltages during the charge and discharge processes. At each voltage step, the cell was held for 10 min at that voltage to guarantee the full extraction/insertion of NH_4^+ in the electrodes. The 6 electrodes obtained at each voltage state were washed with DI water to remove the NH_4Ac electrolyte after disassembling the cells.

A scanning electron microscope, SEM, (LEO 1550 Gemini, Germany) and a transmission electron microscope, TEM, (Talos F200X, Thermo Fisher Scientific, US) were used to examine the microstructure and morphologies of the samples.

X-ray photoelectron spectroscopy, XPS, measurements were performed on the free-standing films using an XPS spectrophotometer (Kratos AXIS UltraDLD, Manchester, U.K.) utilizing monochromatic $\text{Al-K}\alpha$ (1486.6 eV) radiation. The X-ray beam irradiated the film's surfaces at an angle of 45°, using a $300 \times 800 \mu\text{m}^2$ X-ray spot. Charge neutralization was performed using a co-axial, low energy (~0.1 eV) electron flood source to avoid shifts in the recorded binding energy, BE. XPS spectra were recorded for Ti 2p and Mo 3d regions of the $\alpha\text{-MoO}_3/\text{Ti}_3\text{C}_2\text{T}_z$ films, and Mn 2p_{3/2} and N 1s regions of the Mn-based films. The analyzer pass energy for all the regions was 20 eV with a step size of 0.1 eV. The BE scale of all XPS spectra was referenced to the Fermi-edge (E_F), which was set to a BE of zero eV in accordance with reference.^[12] To further confirm the presence of NH_4^+ ions between the MnO_2 interlayers, the $\text{N-MnO}_2/\text{CNTs}$ films were sputtered with Ar^+ ions at 4 keV for 600 s and then at 0.5 keV for 600 s to expose the interior layers. Peak fitting was carried out using XPSPEAK. A Shirley background was used to fit all regions. All peaks were fitted using a Gaussian-Lorentzian line shape.

Electrochemical measurements

All electrochemical measurements were carried out in plastic Swagelok cells and the data were recorded on a potentiostat (VSP, Biologic, France) in 2 and 3-electrode configurations. For the 3-electrode configuration, an activated carbon (YP50F, Kuraray, Japan) disc (with 10 wt.% PTFE binder, 5 mm, ~25 mg cm^{-2}) and

Ag/AgCl in saturated KCl were used as counter and reference electrodes, respectively. Six mm diameter α -MoO₃/Ti₃C₂T_x and N-MnO₂/CNTs discs were used as working electrodes. The AAIBs cells were assembled with the α -MoO₃/Ti₃C₂T_x (pre-cycled at 20 mV s⁻¹ for 10 cycles in a 3-electrode configuration and stopped at -1 V vs. Ag/AgCl) and N-MnO₂/CNTs – without pre-cycling – as anodes and cathodes, respectively. In the full cell, the mass loadings of the α -MoO₃/Ti₃C₂T_x and N-MnO₂/CNTs electrodes were ~1.5 and ~1.9 mg cm⁻², respectively. Before carrying out the electrochemical tests, the full cells were pre-cycled at 20 mV s⁻¹ for 100 cycles to stabilize their performance.

All cell configurations used glassy carbon (GaossUnion, China) as current collectors and glass microfiber membranes (Whatman, General Electric, US) as separators. NH₄Ac (Sigma-Aldrich, ≥98%, Sweden) and DI water with a resistance of 18.2 MΩ cm were used to prepare a 1 M electrolyte.

The gravimetric capacity (mAh g⁻¹) was calculated using the galvanostatic charge-discharge (GCD) technique assuming

$$C_g = I\Delta t / (3.6 \times m) \quad (1)$$

where I (mA) is the current, Δt (s) is the discharge time and m (g) is the weight of electrodes (single electrode for 3-electrode and two electrodes for the full cell).

The gravimetric energy (E_g) and power densities (P_g) were calculated assuming

$$E_g = C_g U / 2 \quad (2)$$

$$P_g = 3.6 \times E_g / \Delta t \quad (3)$$

The volumetric energy (E_v) and power densities (P_v) were calculated assuming

$$E_v = E_g \rho \quad (4)$$

$$P_v = P_g \rho \quad (5)$$

The density of the films was measured assuming

$$\rho = m / (A \times d) \quad (6)$$

where m (g) is the mass of the electrode discs, which are ~0.42 mg and 0.55 mg for anode and cathode, respectively. A (cm²) is the area of the discs, which was ~0.28 cm². d (cm) is the thickness of the electrode discs, obtained from SEM images. For the full cell, the d values were ~13.5 μm and ~6.8 μm for the α -MoO₃/Ti₃C₂T_x and N-MnO₂/CNTs films, respectively. The film densities were thus calculated to be ~1.1 and ~2.8 g cm⁻³ for α -MoO₃/Ti₃C₂T_x and N-MnO₂/CNTs, respectively. All values of specific capacities, densities, etc. were based on the weight of all components in the electrodes, including α -MoO₃, Ti₃C₂T_x, N-MnO₂ and CNTs.

The impedance behavior of the cells was measured using a potentiostat in the 200 kHz to 10 mHz frequency range with a ±10 mV amplitude of potential.

The self-discharge tests were carried out by first holding the cells at 2 V for 0.5 h and then monitoring the cell voltage as a function of time for 10 h. The leakage current was measured by holding the cells at 2 V for 10 h.

The contribution of capacitive- and diffusion-controlled charge storage mechanisms in the electrodes was calculated assuming

$$i = k_1 v + k_2 v^{1/2} \quad (7)$$

in which where $k_1 v$ and $k_2 v^{1/2}$ correspond to the capacitive-controlled and diffusion-controlled processes, respectively.^[13]

Results and Discussion

Phase composition analysis and morphology characterization

The XRD patterns of the α -MoO₃/Ti₃C₂T_x films contain peaks associated with two phases: typical 2D Ti₃C₂T_x and α -MoO₃ (Figure 1a).^[6] Specifically, the high intensity of the (002) plane at 6.9° in the composite films shown in blue in Figure 1a, confirms that at least some of the MXene material is in the form of stacked multilayers, MLs remains. For reasons that are not clear at this time, compared with the pristine MXene films, the (002) peak of the composite films is shifted to lower angles (see blue pattern Figure 1b). The presence of the (020), (040) and (060) peaks of α -MoO₃ (top, blue pattern in Figure 1a) suggests the nanobelts, NBs, are well-ordered along the stacking direction, even in the electrode. As shown in Figure 1(c-e), the basal peaks are slightly shifted to smaller 2θ angles compared with pristine α -MoO₃, indicating expansion of the gap in α -MoO₃ possibly due to the introduction of Ti₃C₂T_x.^[14] Similar results have been reported in our previous work.^[6,15] Other explanations are possible such as changes water content in α -MoO₃ interlayers which slightly shifts the (0 0 l) peaks.

A typical XRD pattern of a T-MnO₂/CNTs film (Figure 1f) is characterized by peaks at 9.4°, 18.8° and 28.2°, that are assigned to (001), (002) and (003) peaks of MnO₂ birnessite, respectively.^[11] The (001) peak at 9.4° corresponds to the interlayer spacing, d , between the octahedral MnO₆ layers of 9.4 Å, that is significantly higher than that of Li⁺, Na⁺ and K⁺ intercalated MnO₂,^[16] but comparable with TMA⁺ intercalated birnessite.^[17] The presence of 3 distinct (00 l) peaks is consistent with our previous work,^[11] indicating good stacking normal to the sheets. The tiny peak at 26.7° belongs to the CNTs.

Immersing the T-MnO₂/CNTs films in the electrolyte for 10 min, shifts the positions of the (00 l) XRD peaks to higher angles (Figure 1g). This is taken to be good evidence for the replacement of the larger TMA⁺ cations with smaller NH₄⁺ ones.^[18] Furthermore, the vanishing of (00 l) ($l > 2$) peaks after ion exchange implies that the exchange disturbs the regularity of the birnessite flakes along the stacking direction.^[19b] The d -value after ion exchange is ≈7.1 Å, which, if we assume the birnessite thickness to be 2 Å,^[11] then the remaining space, ≈5 Å, is more than sufficient to host NH₄⁺ cations with a hydrated radius of ~3.3 Å.^[19]

The fact that typically cathodes used in AAIBs do not contain NH₄⁺ cations and thus require an extra ammoniation step, complicates their production, especially if commercialized.^[7] In our case, the cation exchange is spontaneous and rapid.

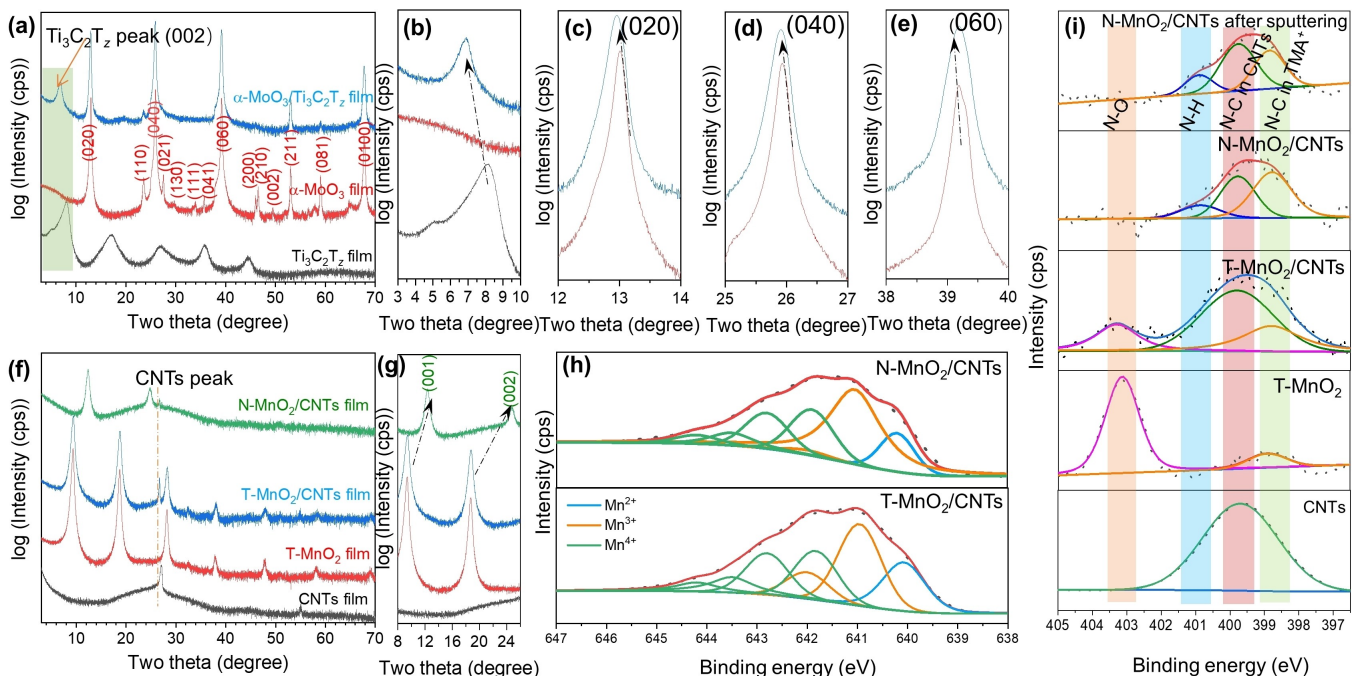


Figure 1. XRD patterns of a) $\text{Ti}_3\text{C}_2\text{T}_z$, $\alpha\text{-MoO}_3$ and $\alpha\text{-MoO}_3/\text{Ti}_3\text{C}_2\text{T}_z$ films; b–e) enlarged area of (a) in different angles; f and g) CNTs, T-MnO₂, T-MnO₂/CNTs and N-MnO₂/CNTs films. h) Mn 2p_{3/2} XPS spectra of T-MnO₂/CNTs and N-MnO₂/CNTs films; i) N 1s XPS spectra of CNTs, T-MnO₂, T-MnO₂/CNTs, N-MnO₂/CNTs and N-MnO₂/CNTs films after sputtering.

The chemical species on the surfaces of the CNTs, T-MnO₂, T-MnO₂/CNTs and N-MnO₂/CNTs films were also investigated by XPS, and the results are shown in Figures 1(h, i), S1 and Tables S1–S3. The Mn 2p_{3/2} spectra of the N-MnO₂/CNTs film in Figure 1(h) are fitted by peaks from Mn²⁺ (640.2 eV), Mn³⁺ (641.1, 641.9 eV) and Mn⁴⁺ (642.0, 642.8, 643.6, 644.2 eV),^[20] confirming a lower-valency for Mn in birnessite. The N 1s peak is detected in all films (Figure 1i). A N signal in the CNTs films is ascribed to the N-containing dispersant *viz.* N-methylpyrrolidone (NMP). The N 1s in the T-MnO₂ film is assigned to N–C in TMA⁺ (398.9 eV) and oxidized N (403.1 eV).^[21] For unknown reasons, the oxidized N peak in the T-MnO₂ films dominates. However, this peak disappears in the T-MnO₂/CNTs films, and a N–H peak (400.9 eV)^[22] appears after soaking in NH₄Ac, confirming the ion exchange between TMA⁺ and NH₄⁺. Note that the N–C peak in TMA⁺ in the N-MnO₂/CNTs films is still present, indicating that a fraction of the TMA⁺ cations are retained. After sputtering the N-MnO₂/CNTs films the fitting results for N (Figure S1 and Table S3), are comparable with those of films that are not sputtered, confirming the presence of NH₄⁺ ions between the MnO₂ interlayers. XPS fitting results of the $\alpha\text{-MoO}_3$ and $\alpha\text{-MoO}_3/\text{Ti}_3\text{C}_2\text{T}_z$ films are shown in Figure S2 and Tables S4–S7. There are no noticeable differences between the two films before and after $\text{Ti}_3\text{C}_2\text{T}_z$ introduction towards Mo 3d. Concomitantly, the increment of TiO₂ content in the total Ti content in the $\alpha\text{-MoO}_3/\text{Ti}_3\text{C}_2\text{T}_z$ film compared with $\text{Ti}_3\text{C}_2\text{T}_z$ is trivial, likely due to the slight surface oxidation during storage.

From SEM micrographs of $\alpha\text{-MoO}_3$ (Figure S3), it is clear that nanobelts ~500 nm wide and more than 100 μm long – are formed. A high-resolution TEM (Figure S4a) micrograph shows a lattice fringe spacing of 0.37 nm, corresponding to the

(002) plane of orthorhombic $\alpha\text{-MoO}_3$. The selected area electron diffraction (SAED) further confirms the presence of the (002), (020) and (110) planes (Figure S4b).

The T-MnO₂ nanosheets, with typical lateral dimension at the micron scale, are folded onto themselves and crumpled (Figure S4c). The intercalated TMA⁺ cations between the flakes are rich in carbon on their surfaces, making it difficult to observe the lattice (Figure S4c). The diffraction patterns in Figure S4(d), however, show their polycrystalline nature, and the rings in the SAED are consistent with the vertical XRD patterns of the films reported previously.^[18] The appearance of sharp spots in the SAED rings (Figure S4d) further confirms the crystalline nature of our flakes.

After filtration of the $\alpha\text{-MoO}_3/\text{Ti}_3\text{C}_2\text{T}_z$ and T-MnO₂/CNTs suspensions, both the as-prepared films are quite flexible (Figure 2a, b). Cross-sectional SEM micrographs of both films exhibit a porous structure (Figure 2d, e). The thicknesses are ~16.5 μm and ~6.8 μm for the $\alpha\text{-MoO}_3/\text{Ti}_3\text{C}_2\text{T}_z$ and T-MnO₂/CNTs films, corresponding to densities of ~1.1 and ~2.8 g cm^{-3} , respectively. The relatively lower density of the $\alpha\text{-MoO}_3/\text{MXene}$ films is ascribed to a more porous structure where the ultralong $\alpha\text{-MoO}_3$ nanobelts presumably prevent the MXene sheets from re-stacking, a perennial problem with electrodes made from 2D sheets.^[23]

After soaking in the 1 M NH₄Ac solution, the N-MnO₂/CNTs films are as flexible as their T-MnO₂/CNTs counterparts. The cross-sectional micrographs also resemble the pristine ones, with a thickness of ~6.8 μm , corresponding to a density of ~2.8 g cm^{-3} .

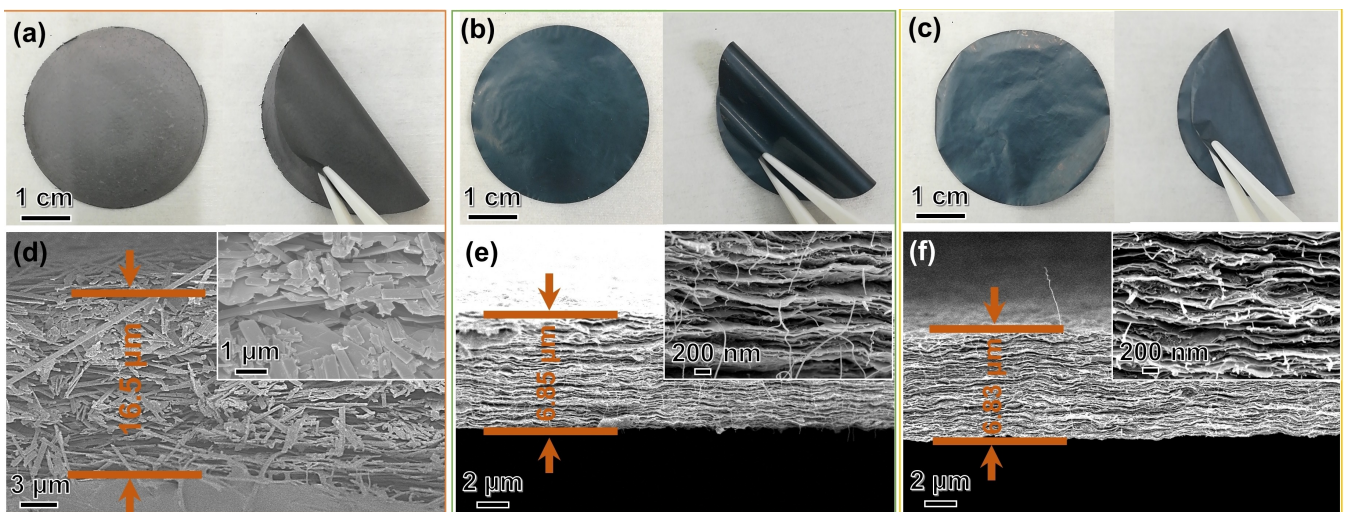


Figure 2. Pictures of a) $\alpha\text{-MoO}_3/\text{Ti}_3\text{C}_2\text{T}_z$, b) T- MnO_2/CNTs , and c) N- MnO_2/CNTs films. Cross-sectional micrographs of d) $\alpha\text{-MoO}_3/\text{Ti}_3\text{C}_2\text{T}_z$, e) T- MnO_2/CNTs and f) N- MnO_2/CNTs films. Insets in d, e and f show higher magnification micrographs.

Electrochemical performance

Typical CV curves for the $\alpha\text{-MoO}_3/\text{Ti}_3\text{C}_2\text{T}_z$ films measured in a 3-electrode configuration, are shown in Figures 3(a) and S5. At all scan rates, the CV curves deviate from a rectangular shape. Small redox peaks are observed at low rates (Figure S5), which probably can be ascribed to the redox reactions for NH_4^+ upon insertion/extraction in the $\alpha\text{-MoO}_3$ structure. Similar results

have been reported for $h\text{-WO}_3$ ^[24] but not $h\text{-MoO}_3$.^[2a] The corresponding GCD curves (Figure 3b) reveal that the capacity of this electrode is 107 mAh g^{-1} ($\sim 117 \text{ mAh cm}^{-3}$) at 0.2 A g^{-1} . When the current density increases to 10 A g^{-1} , a capacity of 31 mAh g^{-1} ($\sim 34.1 \text{ mAh cm}^{-3}$) is still retained. These values are comparable to those previously reported for $h\text{-MoO}_3$ (115, 94 and 44 mAh g^{-1} at 0.1, 1 and 8 A g^{-1} , respectively).^[2a] Unfortunately, this enhancement is somewhat nullified by the low

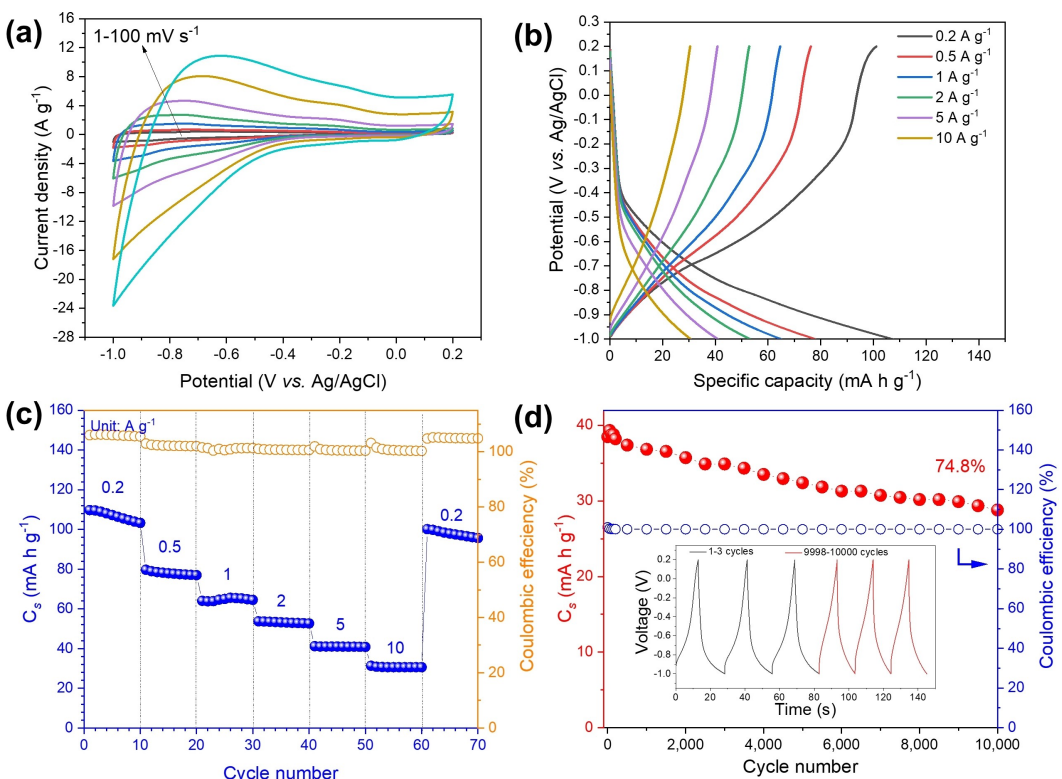


Figure 3. Electrochemical performance of $\alpha\text{-MoO}_3/\text{Ti}_3\text{C}_2\text{T}_z$ film in the 3-electrode configuration: a) CV curves at different scan rates from 1 to 100 mVs^{-1} ; b) GCD curves at different current densities from 0.2 to 10 Ag^{-1} ; c) rate performance; d) cycling performance at 10 Ag^{-1} .

linear fade with cycling over 10,000 cycles at 10 A g^{-1} (Figure 3d). This cyclic fade is also seen at low rates in Figure 3(c). The capacities recover, however when the rate is reduced to 0.2 A g^{-1} again (Figure 3c).

To summarize this section, the $\alpha\text{-MoO}_3/\text{Ti}_3\text{C}_2\text{T}_2$ films exhibit good reversibility at various current densities, with near 100% coulombic efficiency. With cycling, however, the capacity fades almost linearly (Figure 3d).

The electrochemical performance of the N– MnO_2 /CNTs films evaluated using the same 3-electrode configuration is shown in Figure 4. No obvious redox peaks are observed in the CV curves from 20 to 100 mV s^{-1} , and a pair of redox peaks around $0.4/0.7 \text{ V}$ vs. Ag/AgCl are observed at scan rates lower than 20 mV s^{-1} (Figure S6), indicating a pseudocapacitive performance that can be attributed to reversible NH_4^+ intercalation/deintercalation.^[8a] The GCD curves have small plateaus at low current rates (Figure 4b), in accordance with the CV curves. Figure 4(c) shows the effect of rates on capacities: at 0.2 A g^{-1} , a capacity of $\sim 90 \text{ mAh g}^{-1}$ (252 mAh cm^{-3}) is achieved which is slightly lower than that of the Mo-based electrode. When the rate is ramped to 10 A g^{-1} , a capacity of $\sim 18 \text{ mAh g}^{-1}$ (50.4 mAh cm^{-3}) is retained. This value is lower than the Mo-films (Figure 3b). However, when converted into volumetric capacities, these values are comparable due to the higher density of the N– MnO_2 /CNTs films. The rate performance demonstrates good reversibility at different current densities (Figure 4c). The long time cycling performance shows that the capacities increase with cycling and the final capacity retention

is 117.4% (Figure 4d). Here cycling opens up the interlayers exposing new electrochemically active sites.^[25]

In summary, while the N– MnO_2 /CNTs films have relatively lower gravimetric capacities, their volumetric capacities are comparable to the Mo-based films. The cycling stability, however, is quite encouraging and suggests this cathode would work well in AAIBs. It also suggests that if re-stacking can be mitigated, the ultimate capacity could be enhanced further.

Based on charge storage balance theory, *viz.* $m_{-}\text{C}_{-}\text{U}_{-}=m_{+}\text{C}_{+}\text{U}_{+}$ (subscript $+/-$ represent the anode and cathode, respectively), our anode to cathode mass ratio should be ~ 0.76 .^[26] At 2 V, the OCV of our assembled cells is one of the highest values reported for AAIBs. As shown in Figures 5(a) and S7, the CV curves exhibit two pairs of broad peaks at low scan rates, owing to redox reactions for the Mn/Mo upon NH_4^+ extraction/insertion.^[27] Both the negative and positive electrodes fall in their safe potential window at 20 mV s^{-1} (Figure 5b). Otherwise, H_2 evolution or H_2O oxidation occurs.^[28] Based on Equation (3), the capacity of the cell is as high as $\sim 32 \text{ mAh g}^{-1}$ ($\sim 54.1 \text{ mAh cm}^{-3}$) at 0.2 A g^{-1} (Figure 5c). As the current density increases, the capacities reduce to $\sim 20 \text{ mAh g}^{-1}$ ($\sim 33.8 \text{ mAh cm}^{-3}$) at 2 A g^{-1} and $\sim 8 \text{ mAh g}^{-1}$ ($\sim 13.5 \text{ mAh cm}^{-3}$) at 10 A g^{-1} . The coulombic efficiencies (CE) however, are almost $\sim 100\%$ in all cases. The rate performance, shown in Figure 5d, exhibits good reversibility with stable CE. The capacitive-controlled contributions to the overall capacities are shown in Figures 5(e) and S7. Not surprisingly, the capacitive component

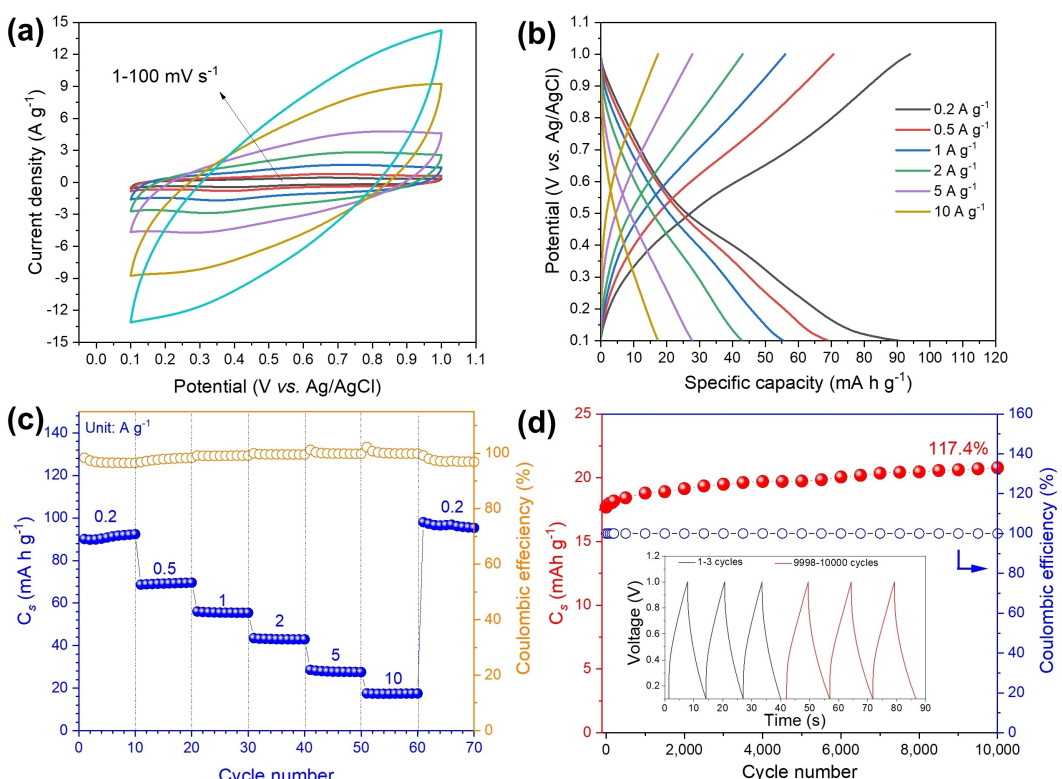


Figure 4. Electrochemical performance of N– MnO_2 /CNTs film in the 3-electrode configuration: a) CV curves at different scan rates from 1 to 100 mV s^{-1} ; b) GCD curves at different current densities from 0.2 to 10 A g^{-1} ; c) rate performance; d) cycling performance at 10 A g^{-1} .

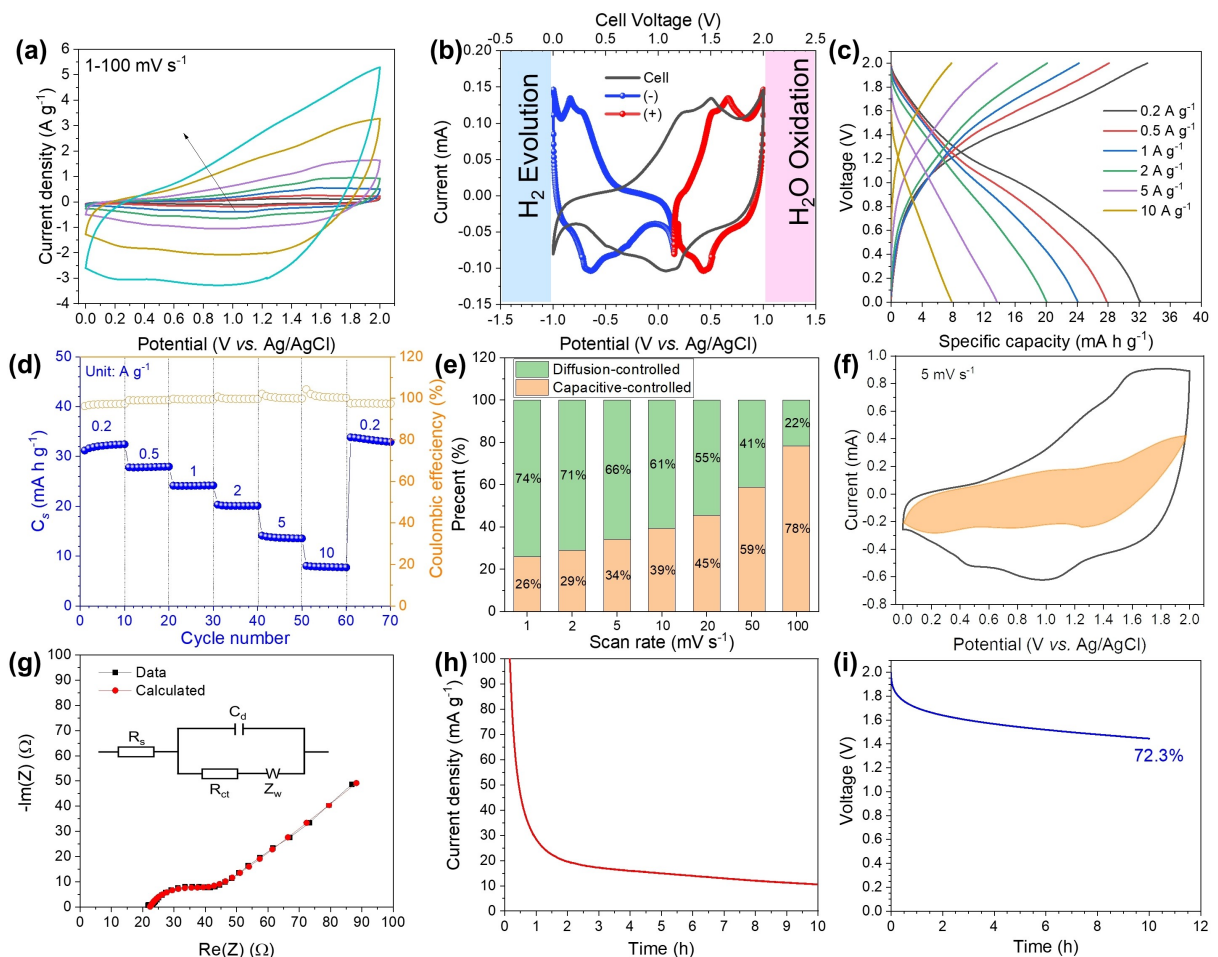


Figure 5. Electrochemical performance of the AAIB full cells: a) CV curves at different scan rates from 1 to 100 mV s⁻¹; b) CV curves of individual electrodes (blue and red) and full cell (black) at 1 mV s⁻¹; c) GCD curves at different current densities from 0.2 to 10 A g⁻¹; d) rate performance; e) capacitive- and diffusion-controlled contributions at different scan rates; f) capacitive-controlled contribution at 5 mV s⁻¹; g) tested and fitted Nyquist plots of the full cell at RT. Inset shows the equivalent circuit used for fitting the Nyquist plots; h) time dependence of leakage current as the cell is held at 2 V; i) SD curve at RT.

increases with increasing scan rates. The low values for the capacitive-controlled part at low scan rates imply that diffusion is preponderant. For example, at 5 mV s⁻¹, the capacitive-controlled contribution is ~34% (see Figure 5f).

Figure 5(g) shows a Nyquist plot, and the fitted parameters are summarized in Table S8. The internal resistances (R_s) and charge transfer resistances (R_{ct}) are 22.3 and 19 Ω, respectively. Furthermore, the slope at low frequencies is tending to 45°, consistent with diffusion being the rate limiting step which agrees well with Figure 5(e).

At ~10 mA g⁻¹, the current leakage is low (Figure 5h). The actual current, not normalized by mass, is ~9.7 μA after 10 h. In comparison, the Ti₃C₂Tz(-)//Mn₃O₄-MnOOH(+) AAASC and Mo_{1.33}CTz//Mo_{1.33}CTz SSC have leakage currents of ~35 mA g⁻¹ and ~30 mA g⁻¹, respectively,^[29] indicating a further advantage of our device.

The self-discharge (SD) performance is shown in Figure 5i. The voltage drops from 2 V to ~1.45 V in 10 h, corresponding to a ~72% retention, which is quite respectable for an aqueous energy storage device. For example, the OCV drops to around 1.15 V from 1.55 V in 10 h for a Mg-ion cell with a retention of

~74%;^[30] the OCV drops from 1.6 V to 1.3 V in 10 h with the retention of ~81% in a “water-in-salt” aqueous Li-ion battery.^[31] Plotting the SD results as a function of $t^{1/2}$ and $\ln t$ in Figure S8(a) and (b), respectively, suggests that a diffusion-controlled process sets in after $t > 2500$ s, with a R^2 value of 0.99 (Figure S8a).

Furthermore, at 1 A g⁻¹, after 2000 cycles, ~73% of the capacity is retained (Figure 6a). When cycling at 10 A g⁻¹ for 43,500 cycles, the specific capacity retention is ~96% (Figure 6b). The XRD patterns of the electrodes after pre-cycling and after cycling at 1 A g⁻¹ for 2,000 cycles are shown in Figure S9(a and b). At this level, there are minor apparent differences that can be attributed to cycling, which is also observed in pre-cycled samples in H₂SO₄.^[32] The relative lower capacity retention at 1 A g⁻¹ is probably due to the self-discharge and the sufficient bulk reactions at such low rates. Based on Equations (2–6), the highest energy density is ~32 Wh kg⁻¹ (~54 Wh L⁻¹) at 0.2 A g⁻¹ and the highest power density is ~10 kW kg⁻¹ (~17 kW L⁻¹) at 10 A g⁻¹, which is outstanding compared with previously reported values shown in Ragone plots (Figure 6c and d).

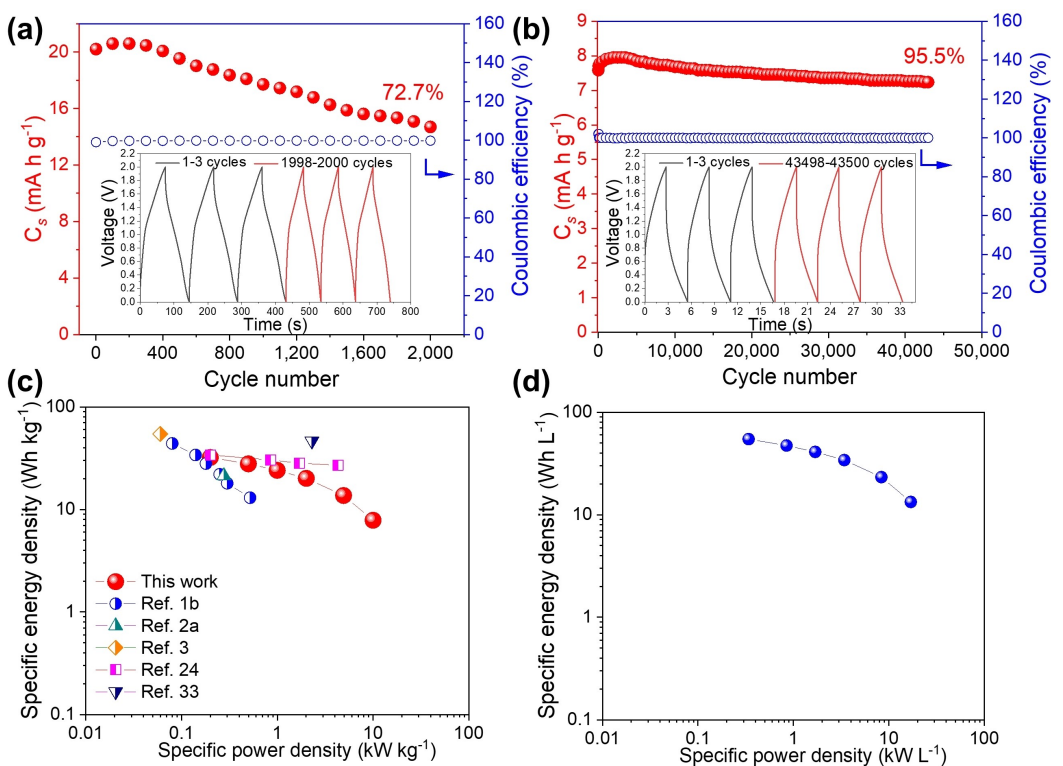


Figure 6. Cycling performance at a) 1 A g^{-1} and, b) 10 A g^{-1} ; Ragone plots in c) gravimetric and d) volumetric values, compared with Refs. [1b,2a,3,24,33]. Note that there are no volumetric results in the literature to compare our results with.

Charge storage mechanism

A schematic of the full cell is shown in Figure 7(a). To reveal the underlying charge storage mechanism of the AAIBs, ex-situ XRD

and XPS characterizations were carried out as a function of the state of charge/discharge of the cells shown in Figure 7(b).

The *ex-situ* XRD patterns obtained at the states of charge/discharge shown in Figure 7(b) in Roman numerals are plotted

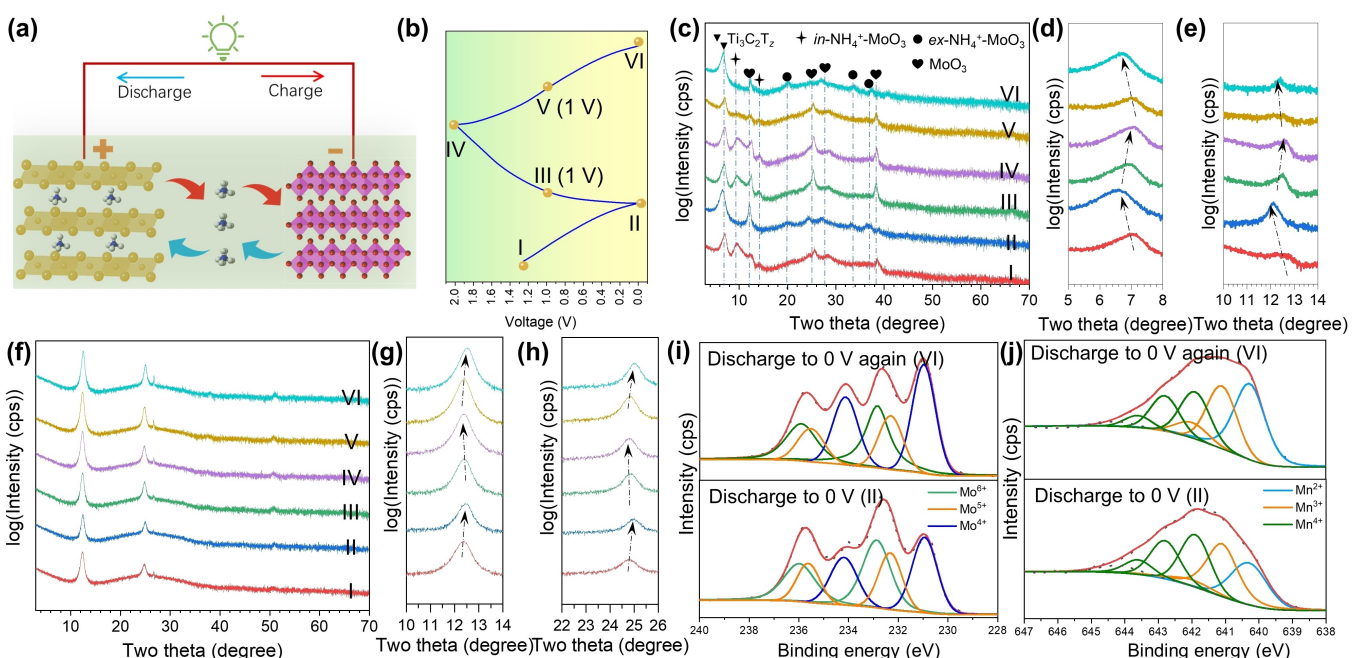


Figure 7. a) Schematic illustration of the full cell; b) GCD curves of the full at 0.5 A g^{-1} ; corresponding *ex-situ* XRD patterns of c–e) $\alpha\text{-MoO}_3/\text{Ti}_3\text{C}_2\text{T}_2$ films and f–h) N–MnO₂/CNTs films; the XPS spectra of i) Mo 3d in $\alpha\text{-MoO}_3/\text{Ti}_3\text{C}_2\text{T}_2$ and j) Mn 2p_{3/2} in N–MnO₂/CNTs films in fully discharged states.

in Figure 7(c). The following information can be gleaned from these results. Upon the first discharge, i.e., going from I to II (Figure 7b) the MXene (002) peaks (Figures 7d and S10a) shift to lower angles. This expansion in turn implies that the cations are holding the MXene layers together and their extraction allows their expansion. Upon the first charge cycle, i.e., going from II to IV, in Figure 7(b), the position of the (002) peak reverts to its original position. In the following discharge process, from IV to VI in Figure 7(b), the (002) peak position reverts to its position upon full discharge. It is thus reasonable to assume that what is happening here is a simple intercalation/deintercalation of NH_4^+ cations between the MXene 2D sheets.

In contradistinction, the situation for the $\alpha\text{-MoO}_3$ phase is different: Figure 7(c) clearly shows that peaks at 9.6° and 14.4° (2θ) only appear when the cell is fully or partially charged (NH_4^+ insertion, i.e., at states I, III, IV and V) and disappear when the cell is fully discharged, *viz.* at II and VI. It follows that the insertion of NH_4^+ into MoO_3 labeled as *in*- NH_4^+ - MoO_3 in Figure 7c; the peaks at 20° and 33.4° , only appear when the cell is fully discharged (NH_4^+ extraction, i.e., at states II and VI) and disappear when the cell is fully or partially charged labeled as *ex*- NH_4^+ - MoO_3 . The natures of *in*- NH_4^+ - MoO_3 and *ex*- NH_4^+ - MoO_3 are unknown at this time. Importantly, the formation of the *in*- NH_4^+ - MoO_3 and *ex*- NH_4^+ - MoO_3 is reversible at least for a few cycles. In addition, the $\alpha\text{-MoO}_3$ (020) peaks show similar trends as those of $\text{Ti}_3\text{C}_2\text{T}_z$, in that they shift to lower angles during discharge and revert during charge (Figures 7e and S10b).

For the cathode, during the initial discharging process (from I to II), the (001) and (002) peaks of N-MnO₂ at 12.4° and 24.8° are shifted slightly to higher angles (Figure 7f-h), implying a decrease in the lattice parameter caused by the strong electrostatic attraction between the inserted NH_4^+ and the lattice O²⁻ in MnO₂.^[8b] Subsequently, those peaks reverse back during de-ammoniation from II to IV and recover to higher angles again during the ammoniation from IV to VI. It follows that the reversible expansion and contraction of the interlayer spacing can be ascribed to the extraction and insertion of NH_4^+ ions.

XPS spectra of the Mo 3d in $\alpha\text{-MoO}_3/\text{Ti}_3\text{C}_2\text{T}_z$ and Mn 2p_{3/2} in N-MnO₂/CNTs films in fully discharged/charged states are shown in Figure 7(i and j). Before assembling the full cell, the $\alpha\text{-MoO}_3/\text{Ti}_3\text{C}_2\text{T}_z$ film was pre-cycled for 10 cycles and stopped at -1 V vs. Ag/AgCl in the 3-electrode configuration. After pre-cycling, the Mo cations were reduced (Figure S11 and Table S9), as evidenced by the increases in the Mo⁵⁺ (232.3, 235.6 eV) and Mo⁴⁺ (230.9, 234.2 eV) contents. After assembling the full cell, the discharge states in II and VI for Mo 3d (Figure 7i, Tables S10 and S11) and Mn 2p_{3/2} (Figure 7j, Tables S12 and S13) are comparable, indicating good reversibility of the two electrodes in full cells. The relatively higher contents of lower-valent Mo and Mn at the stage VI, could be ascribed to the gradually deeper bulk diffusion of NH_4^+ with cycling.

The operating mechanism of the full cell is depicted in Figure 7(a), which is based on the "rocking-chair" insertion/extraction of NH_4^+ between the cathode and anode. Specifi-

cally, during the charging process, NH_4^+ cations are extracted from the pre-ammoniated N-MnO₂/CNTs cathode into the electrolyte, and the Mn²⁺/Mn³⁺ cations are oxidized to Mn⁴⁺. Meanwhile, NH_4^+ is inserted into the $\alpha\text{-MoO}_3/\text{Ti}_3\text{C}_2\text{T}_z$ anode and electrons are transferred through the external circuit. Then, NH_4^+ cations are extracted from the $\alpha\text{-MoO}_3/\text{Ti}_3\text{C}_2\text{T}_z$ and inserted into the N-MnO₂/CNTs anode simultaneously during the discharge process, thus constituting the "rocking-chair" operating mechanism of NH_4^+ , which guarantees the continuous operation of the full cell.

Conclusion

A new aqueous ammonia ion battery was assembled with $\alpha\text{-MoO}_3/\text{Ti}_3\text{C}_2\text{T}_z$ and N-MnO₂/CNTs films as cathodes and anodes, respectively. The introduced $\text{Ti}_3\text{C}_2\text{T}_z$ in $\alpha\text{-MoO}_3$ and the NH_4^+ -rich MnO₂ play crucial roles in the operation of this battery. The OCV of the assembled device is 2 V. At 0.2 A g^{-1} , the specific and volumetric energy densities are $\sim 32\text{ Wh kg}^{-1}$, and $\sim 54\text{ Wh L}^{-1}$ respectively. At 10 A g^{-1} the corresponding values are $\sim 10\text{ kW kg}^{-1}$ and $\sim 17\text{ kW L}^{-1}$. After 10 h, $\sim 72\%$ of the OCV is retained. The charge storage mechanism of our device is due to the shuttling of NH_4^+ cations from one electrode to the other. This work provides a possible roadmap to develop new electrodes for stable and fast aqueous NH_4^+ storage. Before this is possible, however, the self-discharge rate has to be decreased.

Acknowledgements

This work is supported by the Knut and Alice Wallenberg (KAW) Foundation for a Fellowship/Scholar Grant and Project funding (KAW 2020.0033), China Postdoctoral Science Foundation funded project (2020TQ0063, 2021M700759), Jiangsu Planned Projects for Postdoctoral Research Funds, Fundamental Research Funds for the Central Universities and Zhishan Youth Scholar Program of Southeast University.

Conflict of Interest

The authors declare no conflict of interest.

Data Availability Statement

The data that support the findings of this study are available from the corresponding author upon reasonable request.

Keywords: $\alpha\text{-MoO}_3$ · aqueous ammonium-ion batteries · energy and power densities · MnO₂ birnessite · MXene · self-discharge

- [1] a) C. D. Wessells, S. V. Peddada, M. T. McDowell, R. A. Huggins, Y. Cui, *J. Electrochem. Soc.* **2011**, *159*, A98; b) X. Wu, Y. Qi, J. J. Hong, Z. Li, A. S. Hernandez, X. Ji, *Angew. Chem. Int. Ed.* **2017**, *56*, 13026.
- [2] a) G. Liang, Y. Wang, Z. Huang, F. Mo, X. Li, Q. Yang, D. Wang, H. Li, S. Chen, C. Zhi, *Adv. Mater.* **2020**, *32*, 1907802; b) Z. Hai, S. Zhuiykov, *Adv. Mater. Interfaces* **2018**, *5*, 1701385.
- [3] Y. Ma, T. Sun, Q. Nian, S. Zheng, T. Ma, Q. Wang, H. Du, Z. Tao, *Nano Res.* **2022**, *15*, 2047.
- [4] N. A. Chernova, M. Roppolo, A. C. Dillon, M. S. Whittingham, *J. Mater. Chem.* **2009**, *19*, 2526.
- [5] a) M. Ghidiu, M. R. Lukatskaya, M.-Q. Zhao, Y. Gogotsi, M. W. Barsoum, *Nature* **2014**, *516*, 78; b) M. Naguib, M. Kurtoglu, V. Presser, J. Lu, J. Niu, M. Heon, L. Hultman, Y. Gogotsi, M. W. Barsoum, *Adv. Mater.* **2011**, *23*, 4248.
- [6] W. Zheng, J. Halim, A. El Ghazaly, A. S. Etman, E. N. Tseng, P. O. Å. Persson, J. Rosen, M. W. Barsoum, *Adv. Sci.* **2021**, *8*, e2003656.
- [7] J. Han, A. Varzi, S. Passerini, *Angew. Chem. Int. Ed.* **2022**, *61*, e202115046.
- [8] a) Y. Song, Q. Pan, H. Lv, D. Yang, Z. Qin, M.-Y. Zhang, X. Sun, X.-X. Liu, *Angew. Chem. Int. Ed.* **2021**, *60*, 5718; b) Q. Chen, J. Jin, M. Song, X. Zhang, H. Li, J. Zhang, G. Hou, Y. Tang, L. Mai, L. Zhou, *Adv. Mater.* **2022**, *34*, 2107992.
- [9] a) S. Kim, S. Lee, K. W. Nam, J. Shin, S. Y. Lim, W. Cho, K. Suzuki, Y. Oshima, M. Hirayama, R. Kanno, J. W. Choi, *Chem. Mater.* **2016**, *28*, 5488; b) K. W. Nam, S. Kim, S. Lee, M. Salama, I. Shterenberg, Y. Gofer, J.-S. Kim, E. Yang, C. S. Park, J.-S. Kim, S.-S. Lee, W.-S. Chang, S.-G. Doo, Y. N. Jo, Y. Jung, D. Aurbach, J. W. Choi, *Nano Lett.* **2015**, *15*, 4071.
- [10] X. Zhang, M. Xia, T. Liu, N. Peng, H. Yu, R. Zheng, L. Zhang, M. Shui, J. Shu, *Chem. Eng. J.* **2021**, *421*, 127767.
- [11] H. O. Badr, K. Montazeri, T. El-Melegy, V. Natu, M. Carey, R. Gawas, P. Phan, Q. Qian, C. Y. Li, U. Wiedwald, M. Farle, E. Colin-Ulloa, L. V. Titova, M. Currie, T. Ouisse, M. Barbier, A. Rogalev, F. Wilhelm, M. Hans, J. M. Schneider, C. Tandoc, Y.-J. Hu, J. Snyder, M. W. Barsoum, *Mater. Today* **2022**, *54*, 2365-2381.
- [12] G. Grezynski, L. Hultman, *Prog. Mater. Sci.* **2020**, *107*, 100591.
- [13] J. Li, X. Yuan, C. Lin, Y. Yang, L. Xu, X. Du, J. Xie, J. Lin, J. Sun, *Adv. Energy Mater.* **2017**, *7*, 1602725.
- [14] H.-S. Kim, J. B. Cook, H. Lin, Jesse S. Ko, Sarah H. Tolbert, V. Ozolins, B. Dunn, *Nat. Mater.* **2017**, *16*, 454.
- [15] W. Zheng, J. Halim, A. S. Etman, A. E. Ghazaly, J. Rosen, M. W. Barsoum, *Electrochim. Acta* **2021**, *370*, 137655.
- [16] H. Kanoh, W. Tang, Y. Makita, K. Ooi, *Langmuir* **1997**, *13*, 6845.
- [17] R. Zhao, L. Zhang, C. Wang, L. Yin, *J. Power Sources* **2017**, *353*, 77.
- [18] M. Nakayama, S. Konishi, H. Tagashira, K. Ogura, *Langmuir* **2005**, *21*, 354.
- [19] D. Chao, W. Zhou, F. Xie, C. Ye, H. Li, M. Jaroniec, S.-Z. Qiao, *Sci. Adv.* **2020**, *6*, eaba4098.
- [20] M. C. Biesinger, B. P. Payne, A. P. Grosvenor, L. W. M. Lau, A. R. Gerson, R. S. C. Smart, *Appl. Surf. Sci.* **2011**, *257*, 2717.
- [21] a) D. A. Svintsitskiy, L. S. Kibis, D. A. Smirnov, A. N. Suboch, O. A. Stonkus, O. Y. Podyacheva, A. I. Boronin, Z. R. Ismagilov, *Appl. Surf. Sci.* **2018**, *435*, 1273; b) S. Kuroki, Y. Hosaka, C. Yamauchi, M. Sonoda, Y. Nabae, M.-a. Kakimoto, S. Miyata, *J. Electrochem. Soc.* **2012**, *159*, F309; c) D. Geng, S. Yang, Y. Zhang, J. Yang, J. Liu, R. Li, T.-K. Sham, X. Sun, S. Ye, S. Knights, *Appl. Surf. Sci.* **2011**, *257*, 9193; d) G. He, M. Qiao, W. Li, Y. Lu, T. Zhao, R. Zou, B. Li, J. A. Darr, J. Hu, M.-M. Titirici, I. P. Parkin, *Adv. Sci.* **2017**, *4*, 1600214; e) K. N. Wood, S. T. Christensen, D. Nordlund, A. A. Dameron, C. Ngo, H. Dinh, T. Gennett, R. O'Hayre, S. Pylypenko, *Surf. Interface Anal.* **2016**, *48*, 283; f) J. Melke, B. Peter, A. Haberer, J. Ziegler, C. Fasel, A. Nefedov, H. Sezen, C. Wöll, H. Ehrenberg, C. Roth, *ACS Appl. Mater. Interfaces* **2016**, *8*, 82.
- [22] B. Folkesson, *Acta Chem. Scand.* **1973**, *27*, 287.
- [23] a) H. Li, Y. Hou, F. Wang, M. R. Lohe, X. Zhuang, L. Niu, X. Feng, *Adv. Energy Mater.* **2017**, *7*, 1601847; b) M.-Q. Zhao, C. E. Ren, Z. Ling, M. R. Lukatskaya, C. Zhang, K. L. Van Aken, M. W. Barsoum, Y. Gogotsi, *Adv. Mater.* **2015**, *27*, 339; c) L. Qin, Q. Tao, A. El Ghazaly, J. Fernandez-Rodriguez, P. O. Å. Persson, J. Rosen, F. Zhang, *Adv. Funct. Mater.* **2018**, *28*, 1703808; d) F. Zhao, W. Liu, T. Qiu, W.-B. Gong, W. Ma, Q. Li, F. Li, F. Geng, *ACS Nano* **2020**, *14*, 603; e) F. Zhang, X. Guo, P. Xiong, J. Zhang, J. Song, K. Yan, X. Gao, H. Liu, G. Wang, *Adv. Energy Mater.* **2020**, *10*, 2000446.
- [24] Y.-Z. Zhang, J. Liang, Z. Huang, Q. Wang, G. Zhu, S. Dong, H. Liang, X. Dong, *Adv. Sci.* **2022**, *9*, 2105158.
- [25] W. Zheng, J. Halim, L. Yang, H. Badr, Z. Sun, P. O. Å. Persson, J. Rosen, M. W. Barsoum, *Batteries & Supercaps* **2022**, *5*, e202200151.
- [26] Y. Shao, M. F. El-Kady, J. Sun, Y. Li, Q. Zhang, M. Zhu, H. Wang, B. Dunn, R. B. Kaner, *Chem. Rev.* **2018**, *118*, 9233.
- [27] a) S. Wen, J.-W. Lee, I.-H. Yeo, J. Park, S.-i. Mho, *Electrochim. Acta* **2004**, *50*, 849; b) L. Athoué, F. Moser, R. Dugas, O. Crosnier, D. Bélanger, T. Brousse, *J. Phys. Chem. C* **2008**, *112*, 7270.
- [28] J. Park, J. Lee, W. Kim, *ACS Energy Lett.* **2022**, 1266.
- [29] a) W. Zheng, J. Halim, Z. Sun, J. Rosen, M. W. Barsoum, *Energy Storage Mater.* **2021**, *38*, 438; b) W. Zheng, P. Zhang, W. Tian, X. Qin, Y. Zhang, Z. M. Sun, *Mater. Chem. Phys.* **2018**, *206*, 270.
- [30] L. Chen, J. L. Bao, X. Dong, D. G. Truhlar, Y. Wang, C. Wang, Y. Xia, *ACS Energy Lett.* **2017**, *2*, 1115.
- [31] L. Suo, F. Han, X. Fan, H. Liu, K. Xu, C. Wang, *J. Mater. Chem. A* **2016**, *4*, 6639.
- [32] H. Zhang, W. Wu, Q. Liu, F. Yang, X. Shi, X. Liu, M. Yu, X. Lu, *Angew. Chem. Int. Ed.* **2021**, *60*, 896.
- [33] H. Li, J. Yang, J. Cheng, T. He, B. Wang, *Nano Energy* **2020**, *68*, 104369.

Manuscript received: September 29, 2022
Revised manuscript received: December 8, 2022
Accepted manuscript online: December 16, 2022
Version of record online: January 18, 2023